Global variability of high nutrient low chlorophyll regions using neural networks and wavelet coherence analysis.

Gotzon Basterretxea[1], Joan S. Font-Muñoz[1], Ismael Hernández-Carrasco[2], Sergio A. Sañudo-Wilhelmy [3]

5 [1] Department of Marine Ecology, Instituto Mediterráneo de Estudios Avanzados, IMEDEA (UIB-CSIC), Miquel Marqués 21, 07190 Esporles, Illes Balears, Spain.
[2] Department of Oceanography and Global Change, Instituto Mediterráneo de Estudios Avanzados, IMEDEA (UIB-CSIC), Miquel Marqués 21, 07190 Esporles, Illes Balears, Spain.
[3] Department of Biological Sciences and Department of Earth Sciences, University of Southern California, Marine Biology
10 and Biological Oceanography, Los Angeles, California 90089-0371, United States.

Correspondence to: Gotzon Basterretxea (gotzon@imedea.uib-csic.es)

Abstract. We examine 20-years of monthly global ocean color data and modelling outputs of nutrients using self-organizing map analysis (SOM) to identify characteristic spatial and temporal patterns of High Nutrient Low Chlorophyll (HNLC) regions and their association with different climate modes. Analyzing the properties of the probability distribution function of the

15 global nitrate to chlorophyll ratio (NO3:Chl), we estimate that NO3:Chl>17 (mmol NO3/mg Chl) is a good indicator of the distribution limit of this unproductive biome that extends over ~25% of the ocean. Trends in satellite-derived surface chlorophyll (0.6 ± 0.4 to $2\pm0.4\%$ yr^{-1}) suggest that HNLC regions in polar and subpolar areas have experienced an increase in phytoplankton biomass over the last decades. However, much of this variation is produced by a foremost climate-driven transition occurring after the year 2010, which resulted in a reduction in the extension of polar HNLC regions and an increase

20 in their productivity. Chlorophyll variations at HNLC regions respond to all three major climate variability signals (Sea Surface Temperature, SST; El Niño Southern Oscillation, ENSO; and Meridional Overturning Circulation, MOC) and their annual and semiannual variabilities are coherent with seasonal temperature variations. At larger scales, ENSO driven variability (2-4 yr) and decadal-scale processes of heat uptake and redistribution by ocean circulation influence the HNLC extension. Our results are indicative of the long-term changes in phytoplankton biomass and productivity in the ocean and suggest global coupling

25 in the functioning of distant biogeochemical regions.

1 Introduction

High nutrient low chlorophyll (HNLC) areas are ocean regions where primary production should be potentially high but phytoplankton biomass remains relatively low and constant despite the perennial nutrient availability for growth (Martin and

30 Fitzwater, 1988; Chisholm and Morel, 1991). They are interesting regions because they challenge the accepted paradigm of a positive relation between macronutrient concentrations and phytoplankton biomass in open waters but, most importantly, because they represent an important fraction of the global ocean carbon budgets and, therefore, of the withdrawal of

atmospheric CO2 (Boyd et al., 2005; de Baar et al., 1995; Martin et al., 1990). It is estimated that HNLC biomes roughly cover between 20 and 30% of the world's oceans (Pitchford and Brintley, 1999; Tyrrel et al., 2005) comprising three major ocean

35   areas; the Subarctic North Pacific (SNP), the Eastern Equatorial Pacific (EEP) and most of the Southern Ocean (SO) (Coale et al., 1996; Martin, 1990; Parekh et al., 2005).

Because nitrogen is the mineral nutrient needed in greatest abundance by phytoplankton and owing to its generalized depletion in surface waters over much of the oceans, it is considered a key limiting nutrient for ocean production. In HNLC regions, where nitrogen is in excess, other non-exclusive factors such as rapid top-down control by zooplankton grazing, low irradiance,

40   limitations by silicic acid availability, and/or iron (Fe) limitation, have been hypothesized to explain the persistently low chlorophyll (Chl). While these factors may contribute in different degrees to the observed low Chl and determine the phytoplankton dynamics in HNLC regions (see Chavez et al., 1991; Coale et al., 1996; Cullen, 1995; Dugdale and Wilkerson, 1998; Landry et al., 2011), it is generally acknowledged that Fe availability is central to the productivity of HNLC regions (Boyd et al., 2007). All HNLC regions share a chronic Fe-depletion in surface waters and experimental results show highly

45   positive productivity responses to Fe addition (Boyd et al., 2000, 2004; Coale et al., 2004; Martin et al., 1994; Tsuda et al., 2003). Indeed, iron is required in the largest amounts than any of the trace metals for several metabolic processes, and not surprisingly, it has been considered as the ultimate limiting nutrient (Moore and Doney, 2007). This has led to propose a conceptual model of phytoplankton nutrient limitation in the modern ocean based on two functioning regimes, one in which the supply of nutrients is relatively slow and nitrogen availability limits productivity and a complementary regime, with

50   enhanced nutrient supply, where Fe often limits productivity (Moore et al., 2013).

Iron limitation influences the uptake of nitrogen thereby explaining the unused nitrate concentrations in HNLC regions. Indeed, it has been proposed that a delicate balance between nitrogen and Fe availability modulates phytoplankton growth and that co-limitation is rather ubiquitous in the sea (Browning et al., 2017; Bryant, 2003). Other oligoelements and compounds such as B-vitamins, which are also scarce in Fe limited areas, can as well be co-limiting for phytoplankton growth at HNLC regions

55   (e.g. Bertrand et al., 2012; Koch et al., 2011). For example, it has been experimentally observed that the addition of Fe and B12 to Antarctic phytoplankton assemblages can synergistically increase phytoplankton growth (Bertrand et al., 2011; Cohen et al., 2017).

Despite their relevance for global ocean productivity and carbon fluxes, HNLC regions remain loosely defined and knowledge on their temporal and spatial variability and trends is limited. Moreover, their behavior in a global warming scenario is

60   uncertain and may critically depend on coarsely known aspects such as phytoplankton community composition shifts or Fe-cycling rates (Fu et al., 2016; Lauderdale et al., 2020). The original description of HNLC systems by Minas et al. (1986) referred to a slowly growing phytoplankton standing stock despite the presence of high nutrient concentrations. However, there is no rigid criteria accurately defining the functioning of these ecosystems. Several ecosystem characteristics such as species composition, biological structure, carbon utilization pathways, and response to climate change also differ between the HNLC

65   and other ecosystems, reflecting differences in the limiting factor (e.g. Falkowski et al., 1998; Ono et al., 2008).

Of particular interest are the aspects related to the reduced variability and high permanence (i.e. temporal persistence) typically characterizing large HNLC regions. These features are distinctive from those of highly variable systems, which may temporarily present HNLC conditions. For example, some light limited regions in high latitudes may present low productivity and enhanced nutrients during winter but it responds to a transient situation that does not correspond to the generally accepted

70 HNLC paradigm. Similarly, high nutrients and low Chl have been observed at the end of the spring bloom in some productive systems (Nielsdóttir et al., 2009) and in some areas located in coastal upwelling regions (Eldridge et al., 2004; Firme et al., 2003; Hutchins et al., 1998, 2002). While complying with the necessary conditions of high nutrient and low Chl, it is arguable if these ephemeral systems share structural and functioning similitudes with the large HNLC regions.

At a time when understanding biogeochemical responses to large-scale forcings, including climate change, has become a

75 scientific priority, it seems appropriate to revisit some concepts of the functioning of HNLC regions. Their extension and variability are indicative of the dynamic changes in the bidirectional interrelationships of phytoplankton with the environment and with other organisms at large scales. Most of the information on the long-term variations of HNLC regions is depicted from global studies suggesting that their productivity is declining and that they experience prominent interannual to decadal fluctuations superimposed on these long-term trends (i.e. Boyce et al., 2010). Available evidence suggests that some HNLC

80 regions may be decreasing in size as a result of increased ocean stratification (Ono et al., 2008). More recently, Yasunaka et al., (2016), determined that surface trends of phosphate and silicate in the North Pacific are associated with the shoaling of the mixed layer, reporting a positive North Pacific Gyre Oscillation (NPGO) and nutrient correlation. Some studies have shown that oligotrophic areas in the northern hemisphere are expanding between 0.8 and 4% per year, with a faster increase in winter months (Polovina et al., 2008). However, with some exceptions (e.g. Radenac et al., 2012; Yasunaka et al., 2014), specific

85 long-term studies on HNLC regions are scarce and knowledge on their variability at the global ocean scale and their response to climate change remain uncertain.

The objective of this paper is to provide a quantitative assessment of the large-scale patterns of variability of the three major HNLC regions (SNP, EEP and SO) and their relationship with the main modes of climate variability. The study is based on the analysis of 20-year time series of monthly global ocean color data and nutrient outputs from a biogeochemical model using

90 machine learning techniques and wavelets analysis. First, based on the statistical analysis of global NO3:CHL ratios, we determine a robust quantitative criterion to objectively define HNLC regions. Then we characterize the temporal variability patterns of HNLC regions based on their NO3 and Chl concentrations by using Self-Organizing Map (SOM) technique. We use the herein established statistical criterion to assess the spatial variations of HNLC regions over the study period unveiled from the SOM analysis in the spatial domain of NO3:Chl ratios. Finally, through a wavelet coherence analysis (WCA), we

95 quantify the spectral power and the dynamic relationship between the observed Chl variability and three main forcings; Sea Surface Temperature (SST); El Niño Southern Oscillation (ENSO); and Meridional Overturning Circulation (MOC) indices. We show that the combination of WCA with SOM derived characteristic time-series is an especially suitable tool for the analysis of driver-response relationships in the ocean.

2 Materials and Methods

2.1 Ocean color data

100

We employ 20 years of monthly global composites of satellite Chl Level-3 products, derived from merging SeaWiFS, MERIS, MODIS AQUA and VIIRS sensors using a GSM algorithm (Maritorena and Siegel, 2005), obtained from GlobColour data set (www.globcolour.info). The chlorophyll product is spatially gridded, and the weighted average of the different merged Level-2 products is then calculated. The composites have a 0.25° spatial resolution and cover the period from January 1998 to

105 December 2017. We excluded results at the Arctic Ocean and in the coastal Southern Ocean due to the interference of ice cover and prolonged gaps in the data. A total of 654395 pixels were considered in the analysis. We are aware that the consistency of merged multi-mission ocean color satellite series may suffer from some limitations influencing long trend analysis (Mèlin, 2016; Mèlin et al., 2017). However, no significant increase or decrease is observed in the first order trends of GlobColour data more recent studies (e.g. Moradi 2020; 2021). Therefore, while recognizing that some differences in regional

110 and seasonal biases may occur in unified data products and, acknowledging that discontinuities and trends of the median with time should be interpreted carefully according the sensors used (Garnesson et al., 2019), merged Chl can be generally considered a good indicator to describe the value overall phytoplankton trend.

2.2 Nitrate data

Since nutrient observations are still too scarce to allow obtaining time-resolved global-scale fields, we used global NO3

115 obtained from biogeochemical hindcast model provided by Mercator-ocean (http://marine.copernicus.eu). It consists of monthly mean fields of several biogeochemical variables at 0.25° horizontal resolution over the global ocean obtained using the PISCES model (Aumont, 2015). The model is forced by daily mean fields of ocean, sea ice, and atmospheric conditions. Ocean and sea ice forcings are obtained from the numerical simulation FREEGLORYS2V4 produced at Mercator-Ocean and the source of atmospheric forcings is the ERA-Interim reanalysis produced at ECMWF. Initial conditions are set from the

120 World Ocean Atlas 2013 climatology. Complete model description can be found at (http://cmems-resources.cls.fr/documents/). We compared available observational nutrient data (NO3) from the upper 20 m of the water column, obtained by merging bottle cast data from World Ocean database (WOD18, Boyer et al., 2018; https://www.nodc.noaa.gov/), with model results. Generally, we found good agreement between nitrate *in situ* data and model results (r^2=0.98). Main deviations occur in the Southern Ocean and in some coastal areas affected by river runoff. Inference of phytoplankton Fe-stress from satellite ocean

125 color data has been attempted but it is a methodology still presenting large uncertainties (Browning et al., 2014). Therefore, since Fe global fields are not reliable, we assume that excess of NO3 in surface oceanic areas is indicative of Fe limitation for the purpose of this study. We are aware that while iron generally limits productivity where subsurface nutrient supply is enhanced (e.g. Moore et al. 2013), Fe concentrations are more variable than NO3. Consequently, the definition of HNLC regions based on NO3 fields should be more smoothed than those based on Fe-limitation.

2.3 Climatological data

130

Data of SST and climatological indices were obtained from available databases. The SST series at each region was obtained from global observed ocean physics data ARMOR3D (merging satellite and in situ observations) provided by Copernicus Marine Service (http://marine.copernicus.eu). Bi-monthly Multivariate El Niño Southern Oscillation Index (MEI.v2), hereafter ENSO index, was obtained from the National Oceanic and Atmospheric Administration National Center for Environmental

135 Prediction website (https://www.esrl.noaa.gov/psd/enso/mei/). MOC data (Smeed et al., 2019) for the period (2001-2018) was obtained from the RAPID-WATCH MOC monitoring project (www.rapid.ac.uk/rapidmoc).

2.4 Identification of HNLC regions

Presently, the best approximation to define the global distribution of HNLC regions in the world ocean is the use of NODC maps of surface nutrients (https://www.nodc.noaa.gov/). However, excess nutrients availability does not necessarily reflect

140 HNLC conditions. In situ experiments are capable to discern Fe limitation conditions but a more manageable metric to assess the limits on the spatial extent of HNLC regions is required, in particular for remote sensing applications, as well as for allowing objective comparison between different environmental scenarios and studies.

To obtain a quantitative criterion for the definition of HNLC regions, we analyze the values of NO3:Chl ratios obtained from the SOM analysis on the time domain over the global ocean throughout the 20 years of data to identify a common statistical

145 behavior representing HNLC conditions. In particular, we analyze the probability density function (pdf) of the extracted SOM NO3:Chl temporal patterns to identify a threshold for defining HNLC conditions. We use the changes in the trend of the standard deviation calculated for each bin of the pdf function set the threshold ratio.

2.5 Time and space domain SOM analyses

We use SOM (Kohonen, 1982) to elucidate spatial and temporal patterns in the complex relationship between nutrients and

150 phytoplankton. SOM is a subtype of artificial neural network that uses an unsupervised machine learning algorithm to process and extract hidden structures in large amount of data. The SOM algorithm is mainly based in a training process through which an initial neural network is transformed by iteratively presenting the input data. In this study, the initial network is composed of a set of neurons or units represented by a weight vector with a number of components equal to the dimension of the input data vector, i.e. number of rows or columns in the Chl and NO3 matrices, depending on whether the analysis is performed in

155 the temporal or in the spatial domain. In each successive iteration, the neuron with the greatest similarity (excited neuron), called Best Matching Unit (BMU), is updated by replacing their values with the Chl and NO3 values of the input sample data. The similarity is estimated by computing the Euclidean distance between components of the input sample and components of the weight vector of the unit. The unit most similar to the input sample is the one with the minimum distance. In the learning process, Chl and NO3 values of the topological neighboring neurons of the excited neuron (BMU) are also updated replacing

160 their values with values determined by a Gaussian neighborhood function. In this study, we use the imputation batch training

algorithm (Vatanen et al., 2015) where the SOM assumes that a single sample of data (input vector) contributes to the creation of more than one pattern, as the whole neighborhood around the best-matching pattern is also updated in each step of training. This yields a more detailed assimilation of particular features appearing on neighboring patterns. A final neural network with the NO3:Chl patterns is obtained after repeating the training process a number of times until a stable convergence of the map

165   is obtained.

For typical satellite datasets, the SOM can be applied to both space and time domains. Here, we have addressed the analysis separately in the time and space domains of the log-transformed NO3 and Chl datasets. In the time domain, we implement a [4x3] joint-SOM analysis of NO3 and Chl using as input weight vectors concatenating the time-series of NO3 and Chl at each pixel, so each neuron corresponds to a characteristic joint NO3 and Chl temporal pattern over the total period of data. Since

170   each pixel has associated a characteristic time series, we can obtain the location of a particular temporal pattern by computing the BMU for each pixel, providing a map of regions of differentiated NO3:Chl temporal variability. For the analysis herein presented only the regions with NO3:Chl>P_{HNLC} are considered (patterns R1 to R5).

An obstacle to the temporal domain analysis at a global scale is the opposed seasonality at both earth hemispheres. The algorithm classifies the time-series at each grid point attending to the period of the signal but does not consider time lags

175   between the time-series. Hence, pixels in the northern and southern hemispheres with a similar significant period in the NO3 and Chl temporal variability are classified in the same regional pattern even if they are in antiphase when the signals are seasonally lagged (6 months delayed). Regionalization is spatially coherent but the seasonal variation in the characteristic pattern that represents the neuron mixes the phenological patterns of both hemispheres. Therefore, to properly analyze the properties and trends of each of the classified regions, we have calculated the mean features of the regions by segregating the

180   grid points corresponding to each pattern obtained from the SOM analysis into the northern, equator, and southern hemisphere (see scheme in Fig. S1). Trends at each region are assessed by decomposing the NO3:Chl time series in a seasonal signal plus a residual component, and computing best-fit linear trends using regression analysis. Statistically significant trends were considered those exceeding the 95% confidence level.

The SOM analysis in the spatial domain [3x3] array, is addressed by using as input data weighted vectors consisting of spatial

185   distributions over the global ocean of NO3:Chl ratios at a particular time. The selection of the number of neurons depends on the complexity of the data, on the features to be examined in the dataset and in the minimization of the errors. In this case, the resulting neurons after the training loop unveil the characteristic patterns describing the spatial variability of the HNLC regions at a global scale. Then, when computing the BMU for each time we designate the extracted characteristic spatial pattern that better describes the spatial distribution of NO3:Chl ratios at each time (P1 to P9), obtaining the time evolution of the

190   characteristic spatial patterns over the period of study.

Because the SOM is based on the similarity computed from the Euclidean distance between samples, the input vectors of the different variables are normalized to the same range, before initializing the SOM computations. This guarantees a consistent comparison of the weights of the components when computing the distance of two vectors.

SOM computations have been performed using the MATLAB© toolbox of SOM v.2.0 (Vensanto et al., 1999) provided by the
195 Helsinki University of Technology (http://www.cis.hut.fi/somtoolbox/). Further information on SOM analysis is provided in
the supplementary materials.

2.6 Combined SOM - wavelet coherence analysis

To assess the response of HNLC regions to global forcings we use an approach based on the wavelet coherence analysis
(WCA) between two time-series (Grinsted et al., 2004). WCA characterizes cross-correlations by identifying the main
200 frequencies, phase differences, and time intervals over which the relationship between the variability of HNLC regions and
the main global forcings considered in this study, SST variations, ENSO, and MOC indexes, is strong. To do so, we first
analyze the variability in both frequency and time of the characteristic time series of NO3:Chl in the different HNLC regions
extracted by the time domain SOM computations and the time series of the global forcings using the continuous wavelet
transform (CWT).
205 Cross-wavelet transform (XWT) provides information on the common power and relative phase in the frequency-time domain
of two time-series. Using the XWT, we determine the cyclic changes at each of the HNLC regions and their relationship with
the global forcings mentioned above. Finally, we quantify the degree of coherence of cross wavelet transform in the time-
frequency space using the wavelet coherence coefficient R^2 that is calculated as the squared absolute value of the smoothed
cross-wavelet spectrum normalized by the product of the smoothed wavelet individual spectra for each scale (Torrence and
210 Compo, 1998; Torrence and Webster, 1999; Grinsted et al. 2004). R^2 is interpreted as a localized correlation coefficient in the
frequency-time domain and it takes values between 0 (no correlation) and 1 (perfect correlation).
We use the MATLAB software package (Grinsted et al., 2004) for wavelet coherence analysis. It should be noted that cross-
wavelet analysis does not establish causative relationships but only allows identifying possible linkages between variables
through the synchrony of their time series.

215 **3 Results and discussion**

3.1 Global HNLC definition criterion

The mean pattern of global ocean color data for the 20 years analyzed reveals the well-known contrast in phytoplankton
biomass between the highly productive areas at high latitudes and upwelling regions, and the pauperized subtropical gyres
where mean values are <0.1 mg m^{-3} (Fig. 1). Low Chl regions generally correspond with low surface NO3 concentrations
220 whereas the opposite relationship (high nitrate and high chlorophyll) is not that common. Indeed, it is mainly restricted to shelf
waters (i.e. coastal upwelling regions and shelf seas), or to the vicinity of islands and other topographical features where
multiple and overlapping sources of other elements, such as trace metals, are abundant (e.g. Boyd and Ellwood, 2010). Only
in the North Atlantic and in eastern regions of the Antarctic Peninsula, Chl is enhanced, at least transiently during the

productive season. Conversely, a large part of surface ocean waters, particularly in the Southern Ocean, corresponds to regions

225 of relatively low Chl concentrations but with excess nitrate (i.e. >4 mmol m⁻³).

Variations in the boundaries of the HNLC regions could provide an integrative view of how changes in the global atmosphere-ocean system influence ocean productivity. However, systematically determining the boundaries of HNLC regions has remained elusive since it requires coherent information of nutrients and Chl fields. The normalized pdf of the NO3:Chl values extracted from the temporal SOM analysis (shown in Fig. S2) displays a bimodal distribution (see, Fig 1c). This suggests two

230 different scenarios in the nitrate-phytoplankton biomass relationships. The normal distribution fitting of the second mode, which corresponds to high nutrient low chlorophyll regions, is characterized with mean and standard deviation values of μ=24.1 and σ=6.7 mmol m⁻³, respectively. A critical NO3:Chl ratio value, separating both modes, can be therefore estimated as $\mu - \sigma$=17.4 mmol mg⁻¹. Consistently, the pdf bulk analysis of its associated standard deviation (std) function also reveals a clear critical value located where the value of the slope clearly varies (Fig. 1b). Both analyses allow establishing a solid

235 statistical criterion to infer a minimum value of NO3:Chl=17 mmol mg⁻¹ for delimiting HNLC regions from other ocean regions, henceforth referred to as PHNLC. While it is tempting to assume some sort of physiological explanation for this critical value, similarly to Redfield or C:Chla ratios, the NO3:Chl ratio is, in fact, revealing an uncoupling between phytoplankton biomass and resource availability, rather than an algal internal equilibrium. It is worth mentioning that while the pdf of the NO3:Chl values obtained from the SOM analysis is bimodal (Fig. 1c), the bulk pdf of the raw NO3:Chl values

240 (i.e. without performing a SOM analysis) is unimodal. This suggests that the SOM technique is able to unravel relevant structures in the data that cannot be identified using classical approaches.

3.2 Spatial boundaries and characteristic patterns of HNLC regions

Systematically determining the boundaries of HNLC regions has remained elusive since requires coherent information of nutrients and Chl fields. Variations in the boundaries of the HNLC regions could provide an integrative view of how climate

245 scale ocean variations influence ocean productivity. From the 12 subregions obtained in the [4 x 3] SOM analysis (Fig. S2a), five correspond to regions with NO3:Chl>P_{HNLC}, and corresponding with the three traditionally reported HNLC regions (Fig. 2 and Table 1). In these subregions (R1 to R5), surface chlorophyll rarely exceeds 0.8 mg m⁻³ and the mean values range between 0.21 mg m⁻³ and 0.5 mg m⁻³. The global extension of these 5 SOM-identified HNLC subregions encompass 25% of the ocean, being the SO (18%) by far the broadest region, whereas SNP and EEP respectively occupy some 4% and 3% of the

250 ocean.

The SO region is the most complex region both due to its extension and because of the oceanographic processes occurring therein. Physical and chemical properties of the SO tend to be across latitude because of the meridional structure of the MOC and due to the rapid zonal redistribution imposed by circumpolar currents (Orsi et al., 1995). The pattern obtained from the coupled SOM analysis reflects this latitudinal variation. Mean Chl in the SO varies from 0.43±0.92 mg m⁻³ in the proximity

255 of the Antarctic continent (R5) to 0.22±0.06 mg m⁻³ at lower latitudes (see Table 1). Major differences among the defined subregions are not only due to Chl mean values but, also, to the intensified seasonal variability at higher latitudes. For example,

seasonality is particularly evident in R5 and, less so, in other polar subregions. Iron stocks in surface waters of the SO are sustained by deep winter mixing (Tagliabue et al., 2014) and, therefore, are influenced by seasonal patterns. Nevertheless, biological processes such as variations in grazing pressure -which may be an important phytoplankton biomass regulator in the SO (Moreau et al. 2020), changes in species composition affecting biomass:Chl ratios or physiological adjustments in cellular pigmentation (Behrenfeld, 2015; Lozier et al., 2011) may also influence the observed seasonality. Moreover, in subregions such as R5, satellite-derived chlorophyll concentration variability is critically affected by the seasonal ice sheet growth and decay, and by other processes such as ice margin blooms that occur as the ice retreats during austral summer (e.g. Arrigo and van Dijken, 2004). Therefore, the subregion bounding the Antarctic continent, while presenting HNLC characteristics for most of the year, exhibits a differentiated dynamic in terms of Chl variability.

In the SNP nutrient concentrations are generally lower (i.e. <17 mmol m^{-3}) than in the SO and biomass is comparatively higher (see Table 1). Indeed, R1 at SNP only achieves the NO3:Chl criterion for HNLC regions during some periods. In addition, a marked seasonal pattern is observed but phenological variations are often masked by the intense short-term variability. This region is also subjected to zonal variations, which are consistent with previous studies describing the western region as more productive and variable (Imai et al., 2002). Although processes that control biological production in this region are still under debate, atmospheric dust deposition and supply from marginal seas through intermediate waters and subsequent vertical turbulent diapycnal mixing caused have been identified as major Fe sources (Nishioka et al., 2020; Serno et al., 2014). A difference between the SNP and the latitudinally corresponding North Atlantic region has been attributed to river discharges. It is estimated that 20–50% of the annual river discharge to the Arctic Ocean is exported to the Atlantic Ocean through the East Greenland current. In contrast, the SNP is a more enclosed basin in which ocean productivity importance of advection of Fe from the surrounding marginal regions in the North Pacific (Takeda, 2011), but the process of transformation between particulate and dissolved phases could explain some aspects of the observed productivity (Lauderdale et al., 2020).

Finally, the EEP defined by the SOM analysis is consistent with previous studies of this region (Radenac et al., 2012). The seasonal component of variability is almost absent in the EEP. Patterns between R1 and R2 in EEP are highly coupled and differences are mainly due to biomass and available nitrate concentrations.

An interesting feature depicted from the temporal SOM analysis are the positive trends in Chl experienced at the HNLC regions located in polar areas, suggesting an increase in their productivity. Decadal tendencies are in the range of 0.04 to 0.06 mg m^{-3} decade^{-1} in the most productive subregions (R2 to R5 in SO and R3 in SNP) but become negligible at the equator (Table 1). This agrees with estimations by Hammond et al. (2017) that, using a model with a spatial correlation that improves the accuracy of Chl trend estimates, reported positive trends at high latitudes and not significant tendencies at the equator at the 95% interval. In our case, trend robustness is provided by the coherence in the time series obtained using SOM that uses a classification method based on the similarities in the temporal variability patterns. Therefore, it clusters regions with similar trends and variability. A regional average indicates a Chl increase of 0.6% yr^{-1} in the SNP and a 1.9% yr^{-1} in the SO. In the case of the SO, positive trends are highly influenced by a shift occurring at the end of 2010. This Chl increase, mainly affecting some regions of the southern hemisphere, is not exclusive of oceanic Fe-limited waters, since it has been also observed in the highly

productive Patagonian shelf (Marrari et al., 2017). It is arguable to what extent this shift yielding higher Chl after 2010 is related with satellite data merging. SeaWiFS ended operations in 2010 and MERIS sensor ceased in in April 2012; however, decreases in biomass could be expected from these changes (Grarnesson et al., 2019).

Climate change projections for the 21st century predict declines in global marine net primary production but increasing
295 Southern Ocean productivity (Hauck et al. 2015; Moore et al., 2018). To what extent the observed trends anticipate these changes is dubious since, within the relatively short length of the satellite ocean color time-series, trends are highly influenced by decadal variability, as reported by Henson et al. (2010). Indeed, global biomass shifts like the one observed in 2010, suggest complex non-linear responses of marine ecosystems to global change.

3.3 Spatial variability of HNLC regions

300 The set of 9 coherent spatial patterns resulting from the SOM analysis in the space domain and their respective probabilities of occurrence are shown in Fig. 3. The organization of the maps in the figure reveals a hierarchical classification of the maps or scenarios. Most differentiated patterns, also displaying the highest probability of occurrence (the probability to find a pattern similar to the input data), are located in the corners of the neural network and transitional stages connecting these scenarios fill the center. For example, along the top and left side scenarios (P1, P2, P3 and P4), generally occurring during winter (see
305 Fig. 3 and 4b), the SNP extends over a larger region whereas it is highly reduced in the right patterns (P7, P8 and P9; 3% decrease from mean extension). Conversely, Fe limitation in the SO, as inferred from high NO3:Chl ratios, is markedly enhanced towards the top and right (P4, P5, P7, P8 and P9). The extension of the EEP region displays weak seasonal variation. HNLC area extension and NO3 concentrations are not necessarily coupled since limits also depend on Chl levels. In addition, it should be noted that the patterns in the proximity of the Antarctic continent are, in some cases, not well-defined during
310 winter due to ice cover in this region.

The BMU time-series and the monthly frequency of occurrence of each pattern are shown in Figure 4a and b, respectively. The main feature observed is a marked seasonality in the patterns shown in Figure. 3. The patterns with the highest probability of occurrence, P3 and P9 (100% in April and 70% in July), represent winter and summer situations in the northern hemisphere. P4 and P8 characterize transitions towards these patterns. Other patterns such as P6 and P2 (mostly occurring in winter and
315 summer) are rarer but are more frequent after 2010 (Figure 4a). As discussed below, this variation in HNLC regional patterns (i.e. P3 substitutes P1) suggests an abrupt and major transition towards more productive HNLC regions (higher chl is observed). From the nine spatial patterns shown in Figure 3, we estimated the seasonal and interannual variation in the extension of the HNLC regions. The magnitude of these variations remarkably contrasts between the equatorial and polar regions. While the extension of the EEP varies 8.9% seasonally, the SNP changes in up to 100% (Figure 5). The peak in extension for the SNP
320 corresponds to the boreal spring (63% from mean in March). In the case of the SO, seasonality is mainly driven by changes related with the ice limit at high latitudes. The extension of the HNLC region in the boreal winter is the boreal winter is 25% lower than the mean extension.

The relationship observed in interannual variations in HNLC areas suggest a global scale coupling between the equator and the poles. Good inverse correlation (r=-0.99, n=20) is observed between the interannual variations in the extension of EEP and
325 the SO, and a weaker thought significant relationship exists between the SNP and the EEP (r= -0.75, n=20). Therefore, as the extension of HNLC in polar regions contracts (biomass increases), the equatorial region expands and vice versa. All three regions exhibit a shift in their extension after 2010 (Fig. 5). Both the SNP and the SO decrease after this year (5% and 2.6%) whereas the EEP slightly increases (0.4%). This interrelated variation in the HNLC extension particularly that in the SO, could produce important consequences in terms of CO_2 withdrawal from the atmosphere. Several ocean scale changes occurred in
330 2010, which may be related to the observed changes in the HNLC region extension. For example, rapid warming, salinification, and a concurrent dissolved oxygen decline have been observed at BATS during the 2010s (Bates and Johnson, 2020). There is also evidence indicating that a decadal intensification of Pacific trade winds weakened in 2011 (Bordbar et al., 2019). Trade wind variations in the equatorial pacific region are associated with SST anomalies, weakening of the equatorial divergence, and changes in upper-ocean thermal structure (Bordbar, et al., 2017; England et al., 2014). The relationship between the
335 equatorial wind intensity and the equatorial undercurrent strength is also well established (McPhaden, 1993). These atmospheric changes, affecting the upwelling of Fe at the EEP (and indirectly to other oceanic regions), agree with the hypothesis of Winckler et al. (2016) suggesting that ocean dynamics, not dust deposition, control the equatorial Pacific productivity. In our case, we observe a reduction of the extension of the HNLC region at the EEP during an enhanced wind period (before 2011) and an expansion thereafter (Fig. 5). Connections of this mechanism to high latitude HNLC regions reveal
340 large-scale adjustments with consequences in global ocean productivity.

3.4 Drivers of HNLC region variability

3.4.1 Influence of SST variations

As shown in Figures 6 a and b, the temporal variability of both the characteristic NO3:Chl ratios and SST at each region peaks at 12-month periodicity, being this seasonal modulation more intense and temporally consistent in the case of temperature at
345 high latitudes and weaker in the equator. In fact, during 2002-2004, seasonality in the NO3:Chl ratio in the EEP was non-significant. NO3:Chl ratios in the SO also display a semiannual mode and a transference from annual to semiannual periods since 2010. This spectral shift is consistent with the variation observed in the spatial SOM analysis and compatible with reports of decreasing carbon uptake in the SO after 2011 that are related to variations in local wind strength which are known to vary Fe concentrations due to their effect in upwelling strength (Keppler and Landschützer, 2019; Parekh et al., 2005).
350 The WCA analysis between NO3:Chl ratios and SST reveals the synchrony between these variables (Fig 6c). Here, the intensity of the coherence at the 12-month period is further evidenced. At this temporal scale, both variables are highly anti-correlated (high wavelet coherence but with opposite phase -arrows pointing left-) indicating that NO3:Chl ratios are highest when the temperature is at its lowest value (winter) and when phytoplankton uptake declines due to light limitation. A steady 6 month cross-coherence period is also observed at SO but this signal is irregular at the SNP and at the EEP. Semiannual cycles generally

occur in regions where warming and cooling cycles show different durations. In the case of the SO, the semiannual component has been linked to the cyclonic activity with a greater number of cyclones occurring in spring and fall (Howarth, 1983). Finally, a 4-year periodicity in the coherence signal is also suggested at SNP and EEP; however, the coherence is weak and restricted to a few years (after 2010 at the SNP and the EEP, and from 2002 and 2006 at the SO).

3.4.2 Influence of ENSO

The WCA between NO3:Chl ratio at each HNLC region and ENSO are shown in Figure 7a1 to a3. Generally, small coherence structures are observed at semiannual periods; however, the main coherence pattern corresponds to a band extending in the 2 to 4 years in the SNP and > 2yr in the EEP. This coherence between NO3:Chl and ENSO in the 2-4 year period is particularly clear after the year 2005 when ENSO variability intensified. At the EEP, the coherence between both series expands to periods >4 years but, unlike in the SNP region where NO3:Chl ratio is in-phase with ENSO signal, the signals are strongly anticorrelated in this case (anti-phase: relative phase of 180° between both signals). ENSO is the primary source of the interannual variability in this region and its occurrence is related to the decline in NO3 supply. Sub-decadal fluctuations in Chl in the EEP region displaying a good correlation with the ENSO index have been reported before (Oliver and Irwin, 2008; Boyce et al., 2010). Contrastingly, the SO only shows weak evidence of this relationship which suggests that ENSO is not a major forcing driving the variability of NO3:Chl in this region. This is consistent with reports from Ayers and Strutton (2013) who did not found a significant relationship between nutrients in this region and ENSO events. Similarly, Racault et al. (2017) reported evidence indicating that during Eastern Pacific and Central Pacific types of El Niño events, impacts on phytoplankton were widespread, but tended to be greatest in the tropics and subtropics, encompassing up to 67% of the total ocean affected areas.

It can be argued that differences in the response to ENSO are due to the different nature of the forcings driving nutrient supply at each region. While the EEP and the SNP seem to respond to ENSO-related changes in wind forcing, NO3:Chl ratios in the SO are more stable and respond to annual and semi-annual variations. Coupling between the EEP and the SNP dynamics has been reported before. Qui (2002) observed progressive shoaling of the Alaska gyre caused by a strengthening of the cyclonic circulation. The interannual variability of this gyre was connected to ENSO-related equator-originated sea surface height anomalies. Several large-scale climate pattern indexes are invoked to explain physical and biological fluctuations in the SNP. For example, Di Lorenzo et al., (2008) defined the North Pacific Gyre Oscillation (NPGO), which nicely explains the fluctuations of salinity, nutrients, and chlorophyll related to the circulation in the North Pacific gyre. It is beyond the scope of the present work to assess the relationships of all these indexes with the variability in the extension of HNLC regions. Nevertheless, the proposed climate indexes for the Pacific present a high relationship among them, which highlights the strong dynamical linkages between tropical and extratropical modes of climate variability in the Pacific basin, and the important role played by ENSO (Di Lorenzo et al., 2013).

3.4.3 Influence of MOC

As in the case of ENSO, the MOC presents strong seasonal and interannual variations but it is also expected to play a more active role at longer timescales (i.e. decadal and multidecadal; Buckley and Marshall, 2016). Figure 7b shows the MOC transport index (hereafter MOI) measured at 26.5°N (Smeed et al., 2019). Generally, the MOI displays intense interannual variability and, in fact, coherence with NO3:Chl ratios is strongest at interannual time scales (1-1.5 yr; Figures 7b1 to b3). At this timescale, it clearly influences NO3:Chl ratios in the three HNLC regions yet it is more intense in the SO. A stronger MOC should result in the upwelling of macronutrients and Fe at faster rates as well as in increased Ekman transport of nutrients equatorward and subsequent subduction (Ayers and Strutton, 2013). This is observed in the high positive cross-wavelet correlation at 1-1.5 yr in the EEP region. In addition, a clear variation in the coherence phase is observed, being 90º (3-4 months) in the SNP, in phase for the EEP and 270º (9-11 months) phase out at the SO, suggesting a meridional propagation of the MOC effect.

 Figure 7b also reveals a decline of the MOC until 2010 that has remained ~ 15% below its pre-2010 level since then (~17 Sv; Ayala-Solares et al., 2018; Caesar et al., 2018). This trend has been attributed to climate warming and the consequent changes in the hydrological cycle, including sea-ice loss and accelerated melting of the Greenland Ice Sheet, causing further freshening of the northern Atlantic (Bakker et al., 2016; Böning et al., 2016). It has been proposed that AMOC weakening will affect large regions of the world's upper oceans that are currently supplied with nutrients by the South Antarctic Mode Water (Schmittner, 2005).

Weakened MOC after 2010 and, the particularly low value during that year (Fig. 7b), is coincident with the shift in the extension of the HNLC regions shown in Figure 5, suggesting that weaker MOC is related to increases in the extension of the EEP and contraction of the SNP and the SO HNLC regions. In the case of the EEP, it could be proposed that a larger equatorial area with Fe deficiency would be associated with a decline in upwelling intensity. It is estimated that the slowing down of the overturning circulation in the Pacific Ocean since the 1970s has generated a decrease in upwelling of about 25% in an equatorial strip between 9° N and 9° S (McPhaden and Zhang, 2002). Nevertheless, the larger HNLC region at the EEP could also be explained by depletion of Fe in the source waters feeding the EUC, as reported by Kaupp et al. (2011).

At high latitudes, the weakening of the AMOC is coherent with a decrease of the extension of the SNP and the SO (Fig. 5). This anomaly, starting in 2009-2010, is a global feature also reflected in the intertropical convergence zone (ITCZ) time series, an atmosphere's energy balance indicator (see Green et al., 2017; Ibanhez et al., 2017), suggesting a strong atmosphere-ocean coupling with impact on ocean productivity. It is not clear how a reduced flow would favor the increase in biomass at high latitudes. While it is plausible that in the case of abrupt and/or permanent variations of AMOC primary production, and hence phytoplankton biomass, will be reduced, it is more unclear how present-day variations influence phytoplankton biomass. It has been proposed that a reduced AMOC from increased precipitation and melting sea ice, could contribute to reduce vertical mixing which may increase productivity in polar regions (Riebesell et al., 2009). Other studies (e.g., Martinez-García et al., 2009), also based on remotely sensed Chl, showed a relationship between AMOC and Chl variations, mainly due to the

420   interaction of the main pycnocline and the upper ocean seasonal mixed layer. In addition, some paleoclimatic studies have demonstrated that AMOC weakening can increase the productivity north from the Polar Front, but only if an increase in the atmospheric soluble Fe flux is considered (Muglia et al., 2018). Paleoceanographical records reveal a strong correlation between proxies of aeolian Fe flux and productivity has been reported in this region (Kumar et al., 1995; Martínez-García et al., 2009) but, in present times, dust deposition in this area has notably varied and this effect is unlikely. Complex ecosystem

425   processes including competition for Fe with bacteria, Fe remineralization rates, and organic complexation processes could determine the phytoplankton response under future scenarios. Further, biomass building up is not only driven by nutrient availability. Changes in biomass can be produced by variations in the thermocline depth affecting the vertical distribution of phytoplankton. Changes in phytoplankton composition, physiological adjustments in cellular pigmentation, and grazing could also modulate Chl variability. Indeed, prevailing foodweb structure may play an important role in Fe fertilization (Schmidt et

430   al., 2016). At larger scales, there are still unresolved questions about the couplings occurring at different temporal scales. For example, MOC variations are known to interact with ENSO variability (Dong et al., 2006; Dong and Sutton, 2007; Timmermann et al., 2007). These connections provide further evidence of the global scale coupling and feedbacks between the atmosphere, the ocean, and global productivity cycles.

5 Conclusions

435   In the present study, we have addressed the analysis of the extension of the HNLC regions, their long-term variability, and the potential drivers of these variations. We have regionalized the global ocean on the basis of the joint NO3 availability and satellite retrieved Chl abundance variability patterns. We also established a statistical criterion to identify HNLC regions from global Chl and NO3 data. While this regionalization is subject to variations depending on the approach considered, it sets the basis for systematic analyses of these regions and their response to climate variations. More generally, our study shows that

440   the combination of time-domain SOM and wavelet coherence analysis provides a powerful framework to identify regional biological responses to global forcings. Indeed, the proposed methodology is especially suited for the assessment of climate-related change of essential ocean variables retrieved from the increasingly improved and longer and longer time series of remote sensing observations.

    As depicted in our results, variations of oceanic phytoplankton are closely connected to variations in global patterns of

445   atmospheric and oceanic circulation through complex processes. We found important interannual variations in the extension of the HNLC regions (up to 5%, Fig. 5) that are related to the intensity of global forcing anomalies. This provides further evidence that long-term projections of ocean productivity should consider these interlinked relations between the atmosphere, the ocean physics, and its influence on nutrient availability. We show that these interactions have a global dimension (i.e. relation between processes at high and low latitudes) and significant decadal-scale variability. In particular, our analysis reveals

450   a shift in phytoplankton biomass and HNLC variation patterns occurring at the end of 2010, which evidences the occurrence

of fast transitions in ocean biogeochemistry. The drivers of these regime shifts deserve further attention since they represent a fundamental part of the long-term variations in the functioning of marine ecosystems.

Finally, the present study highlights the importance of maintaining long and coherent datasets beyond satellite-borne information to be able to disentangle the different components of variability, particularly at long timescales, and to evaluate

455 the impact of climate change on marine ecosystems. Most of the geochemical information at this scale (i.e. nutrient and Fe fields) will probably require further global sampling programs and refined modeling.

Author contributions

Data were processed and analyzed mainly by G.B., J.S.F and I.H-C. Writing by G. B., J.S.F and I. H-C. and S.A.S. The authors declare no competing financial interests.

460 **Funding sources and data references**

This work was partially supported by SIFOMED grant (CTM2017-83774-P) from Ministerio de Ciencia, Innovación y Universidades, the Agencia Estatal de Investigación (AEI) and the Fondo Europeo de Desarrollo Regional (FEDER, UE). G. Basterretxea was supported by Salvador de Madariaga PRX18/00056 scholarship.

All data included in the present study is accessible from the following publicly available repositories: CARINA
465 (https://www.nodc.noaa.gov/ocads/oceans/CARINA/), COPERNICUS (https://marine.copernicus.eu/), ECMWF (https://www.ecmwf.int/), GEOTRACES (https://www.geotraces.org/), GlobColour (www.globcolour.info), MERCATOR (https://cmems-resources.cls.fr/), NERC (https://nerc.ukri.org) and NOAA (https://www.nodc.noaa.gov/).

References

Ayers, J.M., Strutton, P.G.: Nutrient variability in Subantarctic Mode Waters forced by the Southern Annular Mode and ENSO.
470 Geophysical Research Letters, 40, 3419–3423. doi: 10.1002/grl.50638, 2013

Ayala-Solares, J.R., Wei, H.L., Digg, G.R.: The variability of the Atlantic meridional circulation since 1980, as hindcast by a data-driven nonlinear systems model. Acta Geophysica, 66, 1-13. doi: 10.1007/s11600-018-0165-7, 2018.

Bakker, P., Schmittner, A., Lenaerts, J.T.M., Abe-Ouchi. A.: Fate of the Atlantic Meridional Overturning Circulation: strong decline under continued warming and Greenland melting. Geophysical Research Letters, 43, 12252–12260. doi:
475 10.1002/2016GL070457, 2016.

Bates N.R., Johnson, R.J.: Acceleration of ocean warming, salinification, deoxygenation and acidification in the surface subtropical North Atlantic Ocean. Communications Earth & Environment, 1, 33, doi:10.1038/s43247-020-00030-5, 2020.

Behrenfeld, M.J., O'Malley, R.T., Boss, E.S., Westberry, T. K., Graff, J. R., Halsey, K. H.: Revaluating Ocean warming impacts on global phytoplankton. Nature Climate Change, 6, 323–330. doi:10.1038/nclimate2838, 2015.

480 Bertrand E.M., Saito M.A., Lee P.A., Dunbar R.B., et al.: Iron limitation of a springtime bacterial and phytoplankton community in the Ross Sea: implications for vitamin b12 nutrition. Frontiers in Microbiology, 2, 160. doi:10.3389/fmicb.2011.00160, 2011.

Bertrand, E.M., Allen, A.E., Dupont, C.L., Norden-Krichmar, T.M., et al.: Influence of cobalamin scarcity on diatom molecular physiology and identification of a cobalamin acquisition protein. Proceedings of the National Academy of Sciences, 109 (26),
485 E1762-71. doi: 10.1073/pnas.1201731109, 2012.

Böning, C.W., Behrens, E., Biastoch, A., Getzlaff, K. Bamber, J. L.: Emerging impact of Greenland meltwater on deepwater formation in the North Atlantic Ocean. Nature Geoscience, 9, 523–527. doi: 10.1038/ngeo2740, 2016.

Bordbar, M.H., Martin, T., Latif, M., Park W.: Role of internal variability in recent decadal to multidecadal tropical Pacific climate changes. Geophysical Research Letters, 44, 4246–4255. doi: 10.1002/2016GL072355, 2017.

490 Bordbar, M.H., England, M.H., Gupta, A., Santoso, A., et al.: Uncertainty in near-term global surface warming linked to tropical Pacific climate variability. Nature communications, 10, 1990 doi: 10.1038/s41467-019-09761-2, 2019.

Boyce, D.G., Lewis, M.R., Worm, B.: Global phytoplankton decline over the past century. Nature. 466(7306), 591–596. doi: 10.1038/nature09268, 2010.

Boyd, P., Watson, A., Law, C., Abraham, E.R., et al.: A mesoscale phytoplankton bloom in the polar Southern Ocean
495 stimulated by iron fertilization. Nature, 407, 695–702. doi:10.1038/35037500, 2000.

Boyd P., Law C., Wong C, Nohiri Y. et al.: The decline and fate of an iron-induced subarctic phytoplankton bloom. Nature. 428, 549–553. doi:10.1038/nature02437, 2004.

Boyd, P.W., Strzpek, R., Takeda, S., Jackson, G. et al.: Mesoscale iron enrichment experiments 1993-2005: Synthesis and future directions. Science. 315, 612–617. doi: 10.4319/lo.2005.50.6.1872, 2005.

500 Boyd, P.W., Jickells T., Law C.S., Blain S. et al.: The evolution and termination of an iron-induced mesoscale bloom in the northeast subarctic Pacific. Limnology and Oceanography, 50, 1872-1886, 2007.

Boyd, P.W., Ellwood, M.J.: The biogeochemical cycle of iron in the ocean. Nature Geoscience, 3, 675-682. doi: 10.1038/ngeo964, 2010.

Browning, T.J., Bouman, H.A., Moore C.M.: Satellite-detected fluorescence: Decoupling nonphotochemical quenching from
505 iron stress signals in the South Atlantic and Southern Ocean. Global biogeochemical cycles. 28, 510–524. doi:10.1002/2013GB00477, 2014.

Browning, T. J., Achterberg, E.P., Rapp I., Engel A., et al.: Nutrient co-limitation at the boundary of an oceanic gyre. Nature. 551, 242-246. doi:10.1038/nature24063, 2017.

Bryant, D. A.: The beauty in small things revealed. Proceedings of the National Academy of Sciences,100, 9647–9649. doi:
510 /10.1073/pnas.1834558100, 2003.

Buckley, M.W., Marshall, J.: Observations, inferences, and mechanisms of Atlantic Meridional Overturning Circulation variability: A review. Reviews of Geophysics, 54, 54-63. doi: 10.1002/2015RG000493, 2016

Caesar, L., Rahmstorf, S., Robinson, A., Feulner G., Saba, V.: Observed fingerprint of a weakening Atlantic Ocean overturning circulation. Nature 556, 191–196. doi: 10.1038/s41586-018-0006-5, 2018.

515 Chavez, F.P., Buck, K.R., Coale, K.H., Martin, J.H., et al.: Growth rate, grazing, sinking, and iron limitation of equatorial Pacific phytoplankton. Limnology and Oceanography, 36, 1816–1833. doi: 10.4319/lo.1991.36.8.1816, 1991.

Chisholm S.W., Morel F.M.M.: What controls phytoplankton production in nutrient-rich areas of the open sea? American-Society-of-Limnology-and-Oceanography Symposium - 22-24 February 1991 San-Marcos, California – Preface. Limnology and Oceanography, 36, 1507-1965, 1991.

520 Coale, K.H., Johnson K.S., Fitzwater S.E., Gordon R.M., et al.: A massive phytoplankton bloom induced by an ecosystem-scale iron fertilization experiment in the equatorial Pacific Ocean. Nature. 383, 495-501. doi: 10.1038/383495a0, 1996.

Coale, K.H., Johnson K.S., Chavez F.P., Buesseler K., et al.: Southern Ocean iron enrichment experiment: Carbon cycling in high- and low-Si waters. Science. 304, 408– 414. doi: 10.1126/science.1089778, 2004.

Cohen, N.R., Ellis, K.A. Burns, W.G., Lampe, R.H., et al.: Iron and vitamin interactions in marine diatom isolates and natural 525 assemblages of the Northeast Pacific Ocean. Limnology and Oceanography, 62, 2076-2096. doi: 10.1002/lno.10552, 2017.

Cullen, J.J.: Status of the iron hypothesis after the open-ocean enrichment experiment. Limnology and Oceanography, 40, 1336-l343. doi: 10.4319/lo.1995.40.7.1336, 1995.

de Baar, H.J.W., de Jong, J.T.M., Bakker, D.C.E., Löscher, B.M., et al.: Importance of iron for plankton blooms and carbon dioxide drawdown in the Southern Ocean. Nature. 373, 412-415. doi: 10.1038/373412a0, 1995.

530 Di Lorenzo E., Schneider N., Cobb K.M., Chhak K, et al.: North Pacific Gyre Oscillation links ocean climate and ecosystem change. Geophysical Research Letters, 35, L08607. doi:10.1029/2007GL032838, 2008.

Di Lorenzo, E., Combes, V. Keister, J.E., Strub, P.T., et al.: Synthesis of Pacific Ocean climate and ecosystem dynamics. Oceanography. 26, 68–81, doi: 10.5670/oceanog.2013.76, 2013.

Dugdale, R.C., Wilkerson F.P.: Silicate regulation of new production in the equatorial Pacific upwelling. Nature. 391, 270-535 273. doi: 10.1038/34630, 1998.

Eldridge, M.L., Trick, C., Alm, MB, DiTullio, et al.: Phytoplankton community response to a manipulation of bioavailable iron in HNLC waters of the subtropical Pacific Ocean. Aquatic Microbial Ecology, 35, 79-91. doi: 10.3354/ame035079, 2004.

England, M.H., McGregor, S., Spence, P., Meehl, G. A., et al.: Recent intensification of wind-driven circulation in the Pacific and the ongoing warming hiatus. Nature Climate Change, 4, 222–227. doi: 10.1038/nclimate2106, 2014.

540 Falkowski, P.G., Barber, R.T., Smetacek, V.: Biogeochemical controls and feedbacks on ocean primary production. Science. 281, 200-206. doi: 10.1126/science.281.5374.200, 1998.

Firme, G.F., Rue, E.L., Weeks, D.A., Bruland, K.W., Hutchins, D. A.: Spatial and temporal variability in phytoplankton iron limitation along the California coast and consequences for Si, N, and C biogeochemistry. Global Biogeochemical Cycles, 17, 1016. doi: 10.1029/2001GB001824, 2003.

545 Fu, W., Randerson, J.T., Moore, J.K.: Climate change impacts on net primary production (NPP) and export production (EP) regulated by increasing stratification and phytoplankton community structure in the CMIP5 models. Biogeosciences, 13, 5151-5170. doi: 10.5194/bg-13-5151-2016, 2016, 2016.

Grinsted, A., Moore, J.C., Jevrejeva, S.: Application of the cross wavelet transform and wavelet coherence to geophysical time series. Nonlinear Processes in Geophysics, 11, 561-566. doi:10.5194/npg-11-561-2004, 2004.

550 Hammond, M.L., Beaulieu, C., Sahu, S.K., Henson, S.A.: Assessing trends and uncertainties in satellite-era ocean chlorophyll using space-time modeling. Global Biogeochemical Cycles, 31, 1103–1117. doi: 10.1002/2016GB005600, 2017.

Henson, S.A., Sarmiento, J.L., Dunne, J.P., Bopp, L., et al.: Detection of anthropogenic climate change in satellite records of ocean chlorophyll and productivity. Biogeosciences. 7, 621–640. doi: 10.5194/bg-7-621-2010, 2010

Howarth D.A.: An analysis of the variability of cyclones around Antarctica and their relationship to sea-ice extent. Annals of
555 the Association of American Geographers. 73, 519-537. doi:10.1111/j.1467-8306.1983.tb01856.x, 1983

Hutchins, D.A., DiTullio, G.R., Zhang, Y., Bruland, K.W.: An iron limitation mosaic in the California upwelling regime. Limnology and Oceanography, 43, 1037-1054. doidoi: 10.4319/lo.1998.43.6.1037, 1998.

Hutchins D.A., Hare C.E., Weaver R.S., Zhang Y., et al.: Phytoplankton iron limitation in the Humboldt Current and Peru Upwelling. Limnology and Oceanography, 47, 997- 1011. doi: 10.4319/lo.2002.47.4.0997, 2002.

560 Imai, K., Nojiri, Y., Tsurushima, N., Saino, T.: Time series of seasonal variation of primary productivity at station KNOT (44N, 155E) in the sub-arctic western North Pacific. Deep Sea Research Part II: Topical Studies in Oceanography, 49, 5395-5408. doi: 10.1016/S0967-0645(02)00198-4, 2002.

Keppler, L., Landschützer, P.: Regional Wind Variability Modulates the Southern Ocean Carbon Sink. Scientific reports, 9, 7384. doi:10.1038/s41598-019-43826-y, 2019.

565 Koch, F., Marcoval, A., Panzeca, C., Bruland, K. W., et al.: The effects of vitamin B12 on phytoplankton growth and community structure in the Gulf of Alaska. Limnology and Oceanography, 3, 1023–1034. doi: 10.4319/lo.2011.56.3.1023, 2011.

Kohonen, T.: Self-organized formation of topologically correct feature maps. Biol. Cybern. 43, 59-69. doi:10.1007/BF00337288, 1982.

570 Landry M.R., Selph K.E., Taylor A.G., Décima M., et al.: Phytoplankton growth, grazing and production balances in the HNLC equatorial Pacific. Deep-sea Res. II. 58, 524-535. doi: 10.1016/j.dsr2.2010.08.011, 2011.

Lauderdale, J.M., Braakman, R., Dutkiewicz, S., Follows, M.J.: Microbial feedbacks optimize ocean iron availability. Proceedings of the National Academy of Sciences, 117(9), 4842-4849. doi: 10.1073/pnas.1917277117, 2020.

Lozier, S.M., Dave, A.C., Palter, J.B., Geber, L.M. Barber, R. T.: On the relationship between stratification and primary
575 production in the North Atlantic. Geophysical Research Letters, 38, 1–6. doi: 10.1029/2011GL049414, , 2011.

Marrari, M., Piola, A.R., Valla, D.: Variability and 20-Year Trends in Satellite-Derived Surface Chlorophyll Concentrations in Large Marine Ecosystems around South and Western Central America. Frontiers in Marine Science, 21 doi: 10.3389/fmars.2017.00372, 2017.

Martin, J.H., Fitzwater, S.E.: Iron deficiency limits phytoplankton growth in the northeast Pacific subarctic. Nature. 331, 341–343. doi: 10.1038/331341a0, 1988.

Martin, J.H.: Glacial-interglacial CO2 change: the iron hypothesis. Paleoceanography. 5, 1-13. doi: 10.1029/PA005i001p00001, 1990.

Martin, J.H., Fitzwater, S.E., Gordon, R.M.: Iron deficiency limits phytoplankton growth in Antarctic waters. Global Biogeochemical Cycles, 4, 5-12. doi:10.1029/GB004i001p00005, 1990.

Martin, J.H., Coale, K.S., Johnson, K.S., Fitzwater, S.E. et al.: Testing the iron hypothesis in ecosystems of the equatorial Pacific Ocean. Nature. 371, 123–129. doi:10.1038/371123a0, 1994.

McPhaden, M.J.: Trade wind fetch related variations in Equatorial Undercurrent depth, speed, and transport. Journal of Geophysical Research: Oceans, 98(C2), 2555–2559. doi: 10.1029/92JC02683, 1993.

Minas, H. J., Minas, M., Packard, T.T.: Productivity in upwelling areas deduced from hydrographic and chemical fields. Limnology and Oceanography. 31, 1182-1206. doidoi: 10.4319/lo.1986.31.6.1182, 1986.

Moore, C.M., Mills, M.M., Arrigo, K.R., Berman-Frank, I., et al.: Processes and patterns of oceanic nutrient limitation. Nature Geoscience, 6, 701–710. doi: 10.1038/ngeo1765

Moore, J.K., Doney, S.C., 2007. Iron availability limits the ocean nitrogen inventory stabilizing feedbacks between marine denitrification and nitrogen fixation. Global Biogeochemical Cycles, 21, GB2001. doi:10.1029/2006GB002762, 2013.

Moore, J.K., Fu, W., Primeau, F., Britten, G.L. et al.: Sustained climate warming drives declining marine biological productivity. Science, 359 (6380), 1139-1143. doidoi: 10.1126/science.aao6379, 2018.

Moreau, S., Boyd, P.W. Strutton, P.G.: Remote assessment of the fate of phytoplankton in the Southern Ocean sea-ice zone. Nat Commun 11, 3108. doi:10.1038/s41467-020-16931-0, 2020

Nielsdóttir, M.C., Moore, C.M., Sanders, R., Hinz D.J. et al.: Iron limitation of the postbloom phytoplankton communities in the Iceland Basin, Global Biogeochemical Cycles, 23, GB3001, doidoi:10.1029/2008GB003410, 2009.

Ono, T., Shiomoto, A., Saino T.: Recent decrease of summer nutrients concentrations and future possible shrinkage of the subarctic North Pacific high-nutrient low-chlorophyll region. Global Biogeochemical Cycles, 22, GB3027. doi:10.1029/2007GB003092, 2008.

Parekh, P., Follows, M.J., Boyle, E.A.: Decoupling of iron and phosphate in the global ocean. Global Biogeochemical Cycles, 19, GB2020, doi:10.1029/2004GB002280, 2005.

Pitchford, J.W., Brintley, J.: Iron limitation, grazing pressure and oceanic high nutrient-low chlorophyll (HNLC) regions. Journal of Plankton Research, 21, 525-547. doi: 10.1093/plankt/21.3.525, 1999.

Polovina, J.J., Howell, E.A., Abecassis, M.: Ocean's least productive waters are expanding. Geophysical Research Letters, 35. doi: 10.1029/2007GL031745, 2008.

Racault, M.F., Sathyendranath, S., Brewin, R. J. W., Raitsos, et al.: Impact of El Niño variability on oceanic phytoplankton. Frontiers in Marine Science, 4, 133. doi: 10.3389/fmars.2017.00133, 2017.

Radenac, M.-H., Léger, F., Singh, A., Delcroix, T.: Sea surface chlorophyll signature in the tropical Pacific during eastern and central Pacific ENSO events. Journal of Geophysical Research: Oceans, 117, C04007. doi: 10.1029/2011JC007841, 2012.

Serno, S., Winckler G., Anderson, R.F., Hayes, C T. et al.: Eolian dust input to the Subarctic North Pacific. Earth and Planetary Science Letters. 387, 252-263. doi:10.1016/j.epsl.2013.11.008, 2014

Schmittner, A.: Decline of the marine ecosystem caused by a reduction in the Atlantic overturning circulation. Nature. 434(7033), 628-33. doi: 10.1038/nature03476, 2005.

Smeed, D., Moat, B., Rayner, D., Johns, W.E. et al.: Atlantic meridional overturning circulation observed by the RAPID-MOCHA-WBTS (RAPID-Meridional Overturning Circulation and Heatflux Array-Western Boundary Time Series) array at 26N from 2004 to 2018. British Oceanographic Data Centre - Natural Environment Research Council, UK. doi: 10.5285/8cd7e7bb-9a20-05d8-e053-6c86abc012c2, 2019.

Tagliabue, A., Aumont, O., Bopp, L.: The impact of different external sources of iron on the global carbon cycle. Geophysical Research Letters, 41, 920–926. doi: 10.1002/2013GL059059, 2014.

Takeda, S.: Iron and phytoplankton growth in the Subarctic North Pacific. Aqua-BioScience Monographs, 4, 41–93. doi: 10.5047/absm.2011.00402.0041, 2011.

Torrence, C., Compo, G.: A practical guide to wavelet analysis. Bulletin of the American Meteorological society, 79, 61–78. doi: 10.1175/1520-0477, 1998.

Torrence, C., Webster, P.J.: Interdecadal changes in the ENSO-monsoon system. Journal of Climate, 12, 2679-2710. doi: 10.1175/1520-0442, 1999.

Tsuda, A., Takeda S., Saito H., Nishioka J., et al.: A mesoscale iron enrichment in the western subarctic Pacific induces a large centric diatom bloom. Science. 300, 958– 961. doi:10.1126/science.1082000, 2003.

Tyrrell, T., Merico, A., Waniek, J.J., Wong, et al.: Effect of seafloor depth on phytoplankton blooms in high-nitrate, low-chlorophyll (HNLC) regions. Journal of Geophysical Research: Biogeosciences, 110, G02007, doi: 10.1029/2005JG000041, 2005.

Vatanen, T., Osmala, M., Raiko, T., Lagus, K. et al.: Self-organization and missing values in SOM and GTM. Neurocomputing. 147, 60–70. doi: 10.1016/j.neucom.2014.02.061, 2015.

Vesanto, J., Himberg, J., Alhoniemi, E., Parhankangas, J.: Self-organizing map in Matlab: the SOM Toolbox. In: Proceedings of the Matlab DSP conference, Espoo, Finland, Comsol Oy, 1999.

Winckler, G., Anderson, R.F., Jaccard, S.L., Marcantonio, F.: Ocean dynamics, not dust, have controlled equatorial Pacific productivity over the past 500,000 years. Proceedings of the National Academy of Sciences, 113, 6119–6124. doi:10.1073/pnas.1600616113, 2016.

Yasunaka, S., Nojiri, Y., Nakaoka, S., Ono, T. et al.: Mapping of sea surface nutrients in the North Pacific: Basin-wide distribution and seasonal to interannual variability. journal of geophysical research: oceans, 119, 7756–7771. doi: 10.1002/2014JC010318, 2014.

645   Yasunaka, S., Ono, T., Nojiri, Y., Whitney, F.A., et al.: Long-term variability of surface nutrient concentrations in the North
       Pacific, Geophysical Research Letters, 43, 3389-3397. doi:10.1002/2016GL068097, 2016.

650 **Tables**

Table 1. Mean±std characteristics of each of the SOM-defined subregions. NO3 and Chl values are respectively from model and satellite data. Decadal chlorophyll trends (ΔChl) are calculated from the mean time-series of monthly deseasonalized chlorophyll.

Region	Subregion	NO3 (µM)	Chl (mg m-3)	NO3:Chl (mmol NO3 mg Chl^{-1})	ΔChl (mg m^3 decade^{-1})
SNP					
	R1	4.51 ± 1.02	0.31 ± 0.07	15 ± 3	+0.05
	R2	8.05 ± 0.88	0.36 ± 0.07	23 ± 6	+0.26
	R3	15.52 ± 2.27	0.49 ± 0.16	35 ± 15	+0.43
EEP					
	R1	4.04 ± 0.77	0.22 ± 0.02	18 ± 3	+0.01
	R2	6.63 ± 1.42	0.39 ± 0.05	20 ± 4	+0.08
SO					
	R1	4.13 ± 1.05	0.22 ± 0.06	20 ± 4	+0.24
	R2	9.11 ± 1.23	0.31 ± 0.06	31 ± 9	+0.42
	R3	15.73 ± 1.07	0.32 ± 0.10	55 ± 17	+0.47
	R4	23.26 ± 1.06	0.26 ± 0.16	104 ± 32	+0.62
	R5	29.18 ± 1.57	0.43 ± 0.92	103 ± 54	+0.46

655
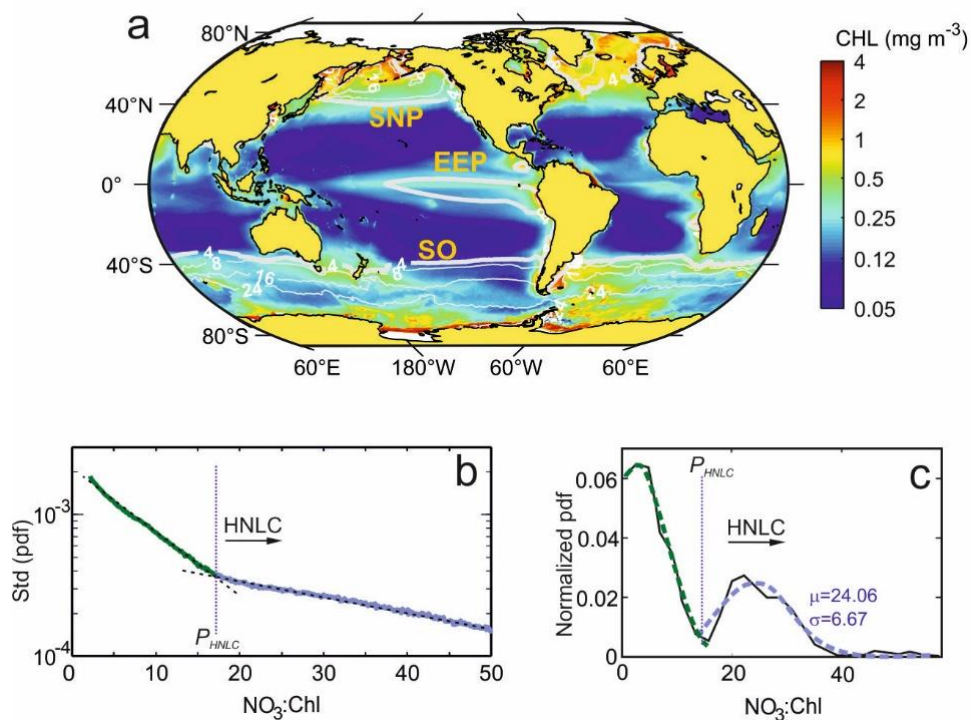
Figures

660 **Figure 1 a) Global mean satellite Chl concentrations for the period 1998-2018 and superimposed surface NO3 contour lines (white) from modeling data (isolines are drawn at 4mmol m-3 intervals). b) Standard deviation of the probability density function (PDF) of the NO3:Chl monthly ratios obtained for the 20 years analyzed. Note that the y-axis scale is logarithmic. c) Normalized probability density function of the values of the NO3:Chl ratio obtained from the SOM temporal patterns. Green and blue lines show the fit to a normal distribution for the first and second pdf modes, respectively. The critical point ratio P$_{HNLC}$ =17 mmolNO3 mgChl^{-1} delimits HNLC regions from macronutrient limited regions.**

665
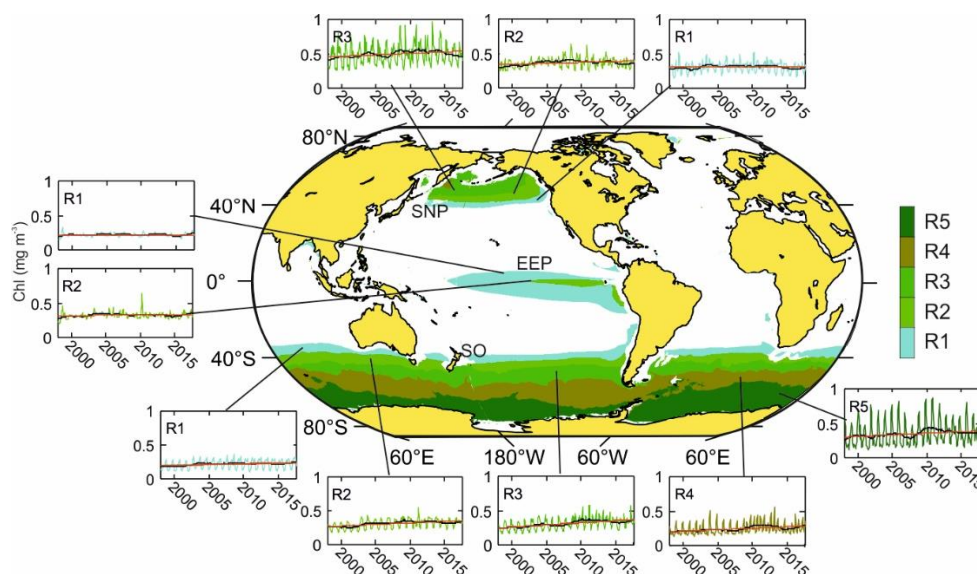
Figure 2 HNLC regions (SNP, EEP, and SO) and corresponding subregions (R1 to R5) obtained from coupled NO3-Chl temporal-SOM analysis. Patterns corresponding to a subregion in the northern and southern hemisphere, present a similar pattern although seasonally lagged (6-month delay). Insets show the time series of the averaged Chl over the corresponding subregion (complete map and NO3:Chl ratios are shown in Fig. S2). The black line represents the 24-month filtered series and the red line indicates the trend (values shown in Table 1).
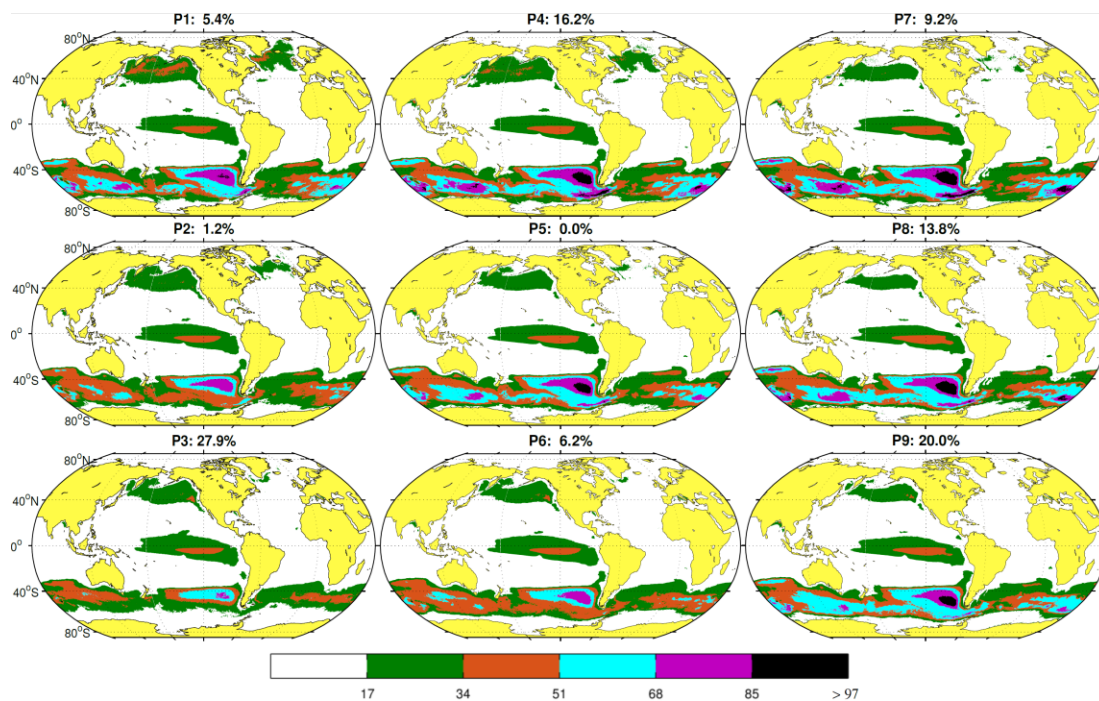
670

Figure 3. Characteristic spatial patterns (P1 to P9) of HNLC regions as defined by NO3:Chl ratios > P_{HNLC}. The value on top of each pattern indicates the probability of occurrence of each pattern over the 20-year period analyzed. To preserve the topology, the SOM algorithm introduces some patterns with zero probability of occurrence, such as P5. The colorbar indicates the different NO3:Chl ranges.
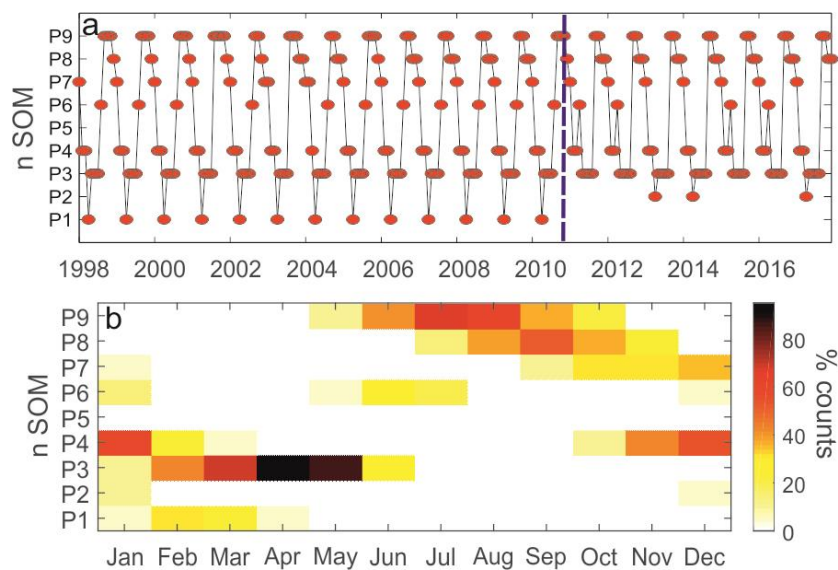
Figure 4. a) Time evolution of the spatial patterns as defined by the Best Matching Units for the period of 1998-2018. The blue dashed line indicates the regime shift occurring after 2010. b) Monthly frequency of occurrence of the spatial patterns identified in Figure 3.
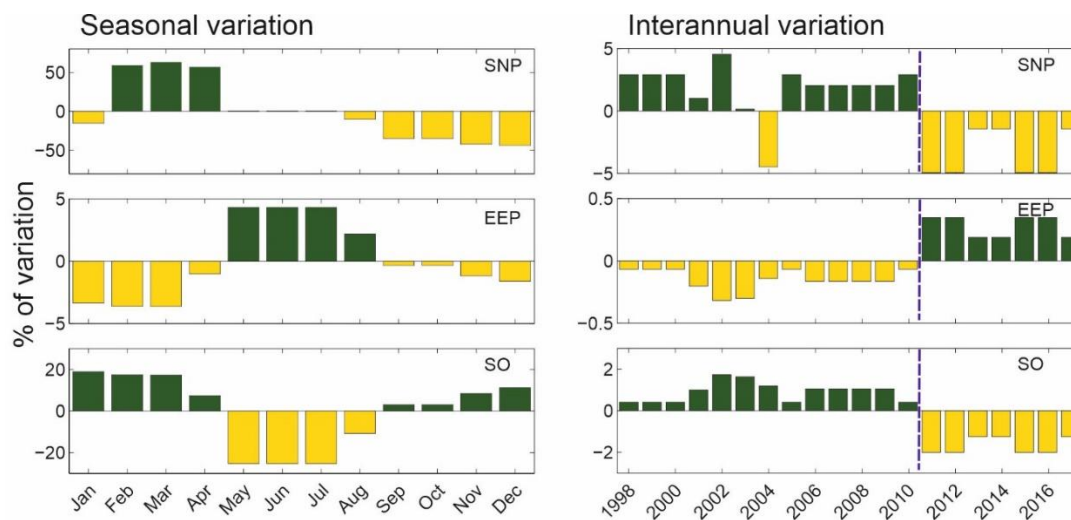
690

Figure 5. Seasonal (left) and interannual variations (right) in the spatial extension of the three HNLC regions. Variations are referred to the mean extension of each region. The blue dashed lines indicate the regime shift occurring after 2010.
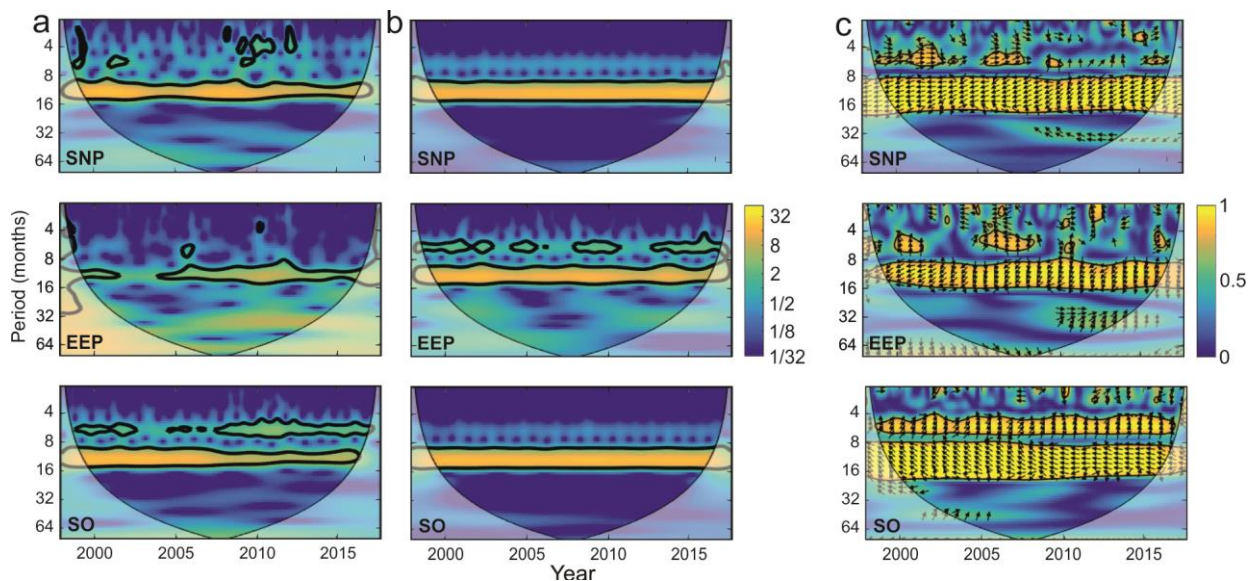
Figure 6. Continuous wavelet spectra (CWT) of a) the NO3:Chl ratio and b) SST, and c) cross-wavelet coherence (CWA) between both series for each of the HNLC regions (SNP, EEP and SO). The thick black contour designates the 95% confidence level and the cone of influence where edge effects are not negligible is shown as a lighter shade. The arrows in (c) indicate the phase relationship between the signals. Arrows pointing right: both signals are in phase; pointing left: in anti-phase; upward: Y leading X by 90º and downward: X leading Y 90º. Period units are months. Note that a lead of 90º can be also interpreted as a lag of 270º or a lag of 90º relative to the anti-phase.
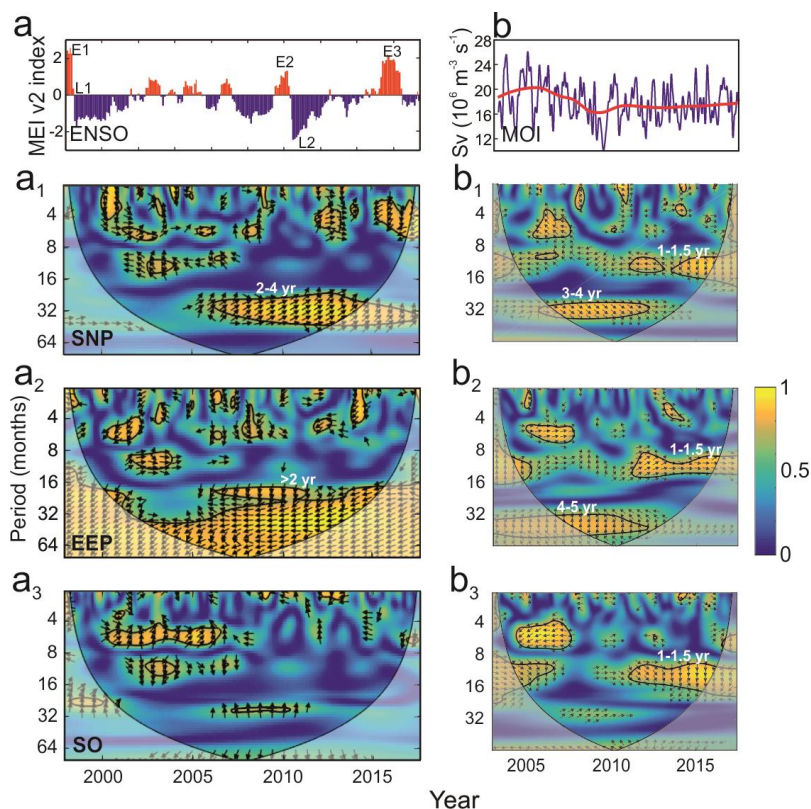
700

Figure. 7. a) ENSO (MEI v2) index. E1-E3 indicate intense El Niño episodes and L1 and L2 mark strong La Niña periods. a1, a2, a3 display the cross-wavelet coherence between NO3:Chla ratio and ENSO for each of the HNLC regions. b) Monthly AMOC transport index for the period (2004-2017) measured at 26.5°N (Smeed et al., 2016). The red line shows the decadal variation. b1, b2, b3 display the cross-wavelet coherence between NO3:Chla ratio and AMOC for each of the HNLC regions. The thick black contours in the cross-wavelet coherence figures designate the 95% confidence levels and the cone of influence where edge effects are not negligible is shown as a lighter shade. The arrows indicate the phase relationship between the signals with the horizontal component indicating in-phase (rightward) or out of phase (leftward) and the vertical component indicating a 90º phase difference lagging (upward) or leading (downward). Period units are months.